Supporting Information

Highly efficient GeSe micro air brick-based thin film standalone solar water splitting photoelectrode with solar light soaking accumulated process

Kang Wang [a, b], Huanyang Ni [a, b], Weidong Zhao [a, b], Xiaomim Wu [a, b], Yucheng Hu [a, b], Guohong Xiao [a, b] and Feng Jiang [a, b, c, d] *

a. Institute of Hydrogen Energy for Carbon Peaking and Carbon Neutralization, School of Semiconductor Science and Technology, South China Normal University, Foshan 528225, China

b. Institute of Semiconductor Science and Technology, South China Normal University, 55 Zhongshan Avenue West, Tianhe District, Guangzhou 510631, China.

c. Chengfeng Light Energy Science and Technology (Guangzhou) Limited Company, Huangpu District, Guangzhou, China

d. Donghai Laboratory, Zhoushan, Zhejiang 316021, China

*E-mail: fengjiangsolar@126.com

Abbreviations define in the manuscript：

photoelectrochemical (PEC)
solar-to-hydrogen efficiency (STH)
micro air brick (MAB)
dual photoelectrode (D4)
photovoltaic-photoelectrochemical (PV-PEC)
perovskite solar cells (PSCs)
dye-sensitized solar cells (DSSCs)
valence band (VB)
conduction band (CB)
rapid box thermal deposition (RBTD)
photothermovoltaic cell (PTV)
thermoelectric generator (TEG)
thermophotovoltaic cell (TPV)
dimensionally stable anode (DSA)
photon-to-electron conversion efficiency (PCE)
atomic layer deposition (ALD)
hydrogen evolution reaction (HER)
oxygen evolution reaction (OER)

Experimental

Fabrication of GeSe Photocathodes

GeSe films were prepared via rapid thermal deposition. 300 mesh GeSe powder (99.999%) was symmetrically placed around the Mo sheet (4 cm × 4 cm) in graphite box, then the graphite box loaded top of AIN plate. Molecular pump was assembled with an RTS tube furnace (MIT, Hefei, China) to maintain the vacuum at 5×10^{-3} pa. The deposition process was first preheated the source and substrate at 350 ℃ for 5 minutes, then quickly increased the source temperature up to 500 ℃ within 10 seconds maintained this temperature for 100 seconds, and finally set a fixed cooling rate of 10 ℃/min until room temperature.

Surface Modification with TiO_2 Layer

Surface modification of the GeSe MABs thin film was performed by LabNano 9100 atomic layer deposition (ALD) system. Titanium tetrakis (dimethylamide) and H_2O were used as titanium and oxygen source, respectively. Based on our empirical value (The deposition rate of the ALD of TiO_2 film was estimated by Spectroscopic ellipsometer measurement), the growth rate was estimated to be about 0.054 nm per cycle and the films were grown for 50 nm at 150℃.

Surface Modification with Pt Catalyst

Pt particles was deposited on the prepared TiO_2/GeSe films by photo-electrodeposition. The deposition was performed by using a three-electrode system consisting of the TiO_2/GeSe sample as a working electrode, a Pt wire as a counter electrode, and Ag/AgCl as a reference electrode. These electrodes were immersed in 0.1 M Na_2SO_4 solution containing 1 mM H_2PtCl_6, and the deposition was performed with a constant potential of -0.1 V vs Ag/AgCl. During the deposition, the TiO_2/GeSe working electrode was illuminated by simulated AM 1.5 solar irradiation.

Thermoelectric generator

A commercial thermoelectric generator (CMD-LH, TEC-33506) have adopted in this work and original geometry of 54 × 62 × 4 mm. The Maximum output voltage and current is 42 V and 6 A, respectively.

PEC Measurements.

An online gas chromatography system (Shimadazu GC-2014C gas analyzer equipped with a MS-5A column and a thermal conductivity detector) was used to detect H_2 amount during the PEC water splitting. The PEC cell was covered by a water jacket to maintain the temperature at 293 K. Two-electrode configuration consist of Pt-TiO_2/GeSe as the working electrode, a DSA electrode as the counter electrode and reference electrode.

Solar to hydrogen efficiency

η_{STH} was calculated by the following equation:

$$\eta_{STH(\%)} = \left[\frac{Chemical\ energy\ produced}{Solar\ energy\ input}\right]$$

$$= \left[\frac{Rate\ of\ H2\ prodection\ \times \Delta G^{H_2O \rightarrow H_2 + \frac{1}{2}O_2}}{Total\ incident\ solar\ power \times Electrode\ Area}\right]$$

$$= \left[\frac{(mmol\ H_2\ per\ s) \times (237000\ J/mol)}{P_{Total}(mW/cm^2) \times Area(cm^2)}\right]_{AM1.5G}$$

$$= \left[\frac{J_{sc}(mA/cm^2) \times (1.23\ V) \times \eta_F}{P_{Total}(mW/cm^2)}\right]_{AM1.5G}$$

$$= \left[\frac{13.8\ mA/cm^2 \times 1.23\ V \times 95\% \times t}{P_{Total} mW/cm^2 \times (t + 300\ s)}\right]$$

where η_F is the Faradaic efficiency of H_2 or O_2 production. J_{sc} is the generated photocurrent density. The light intensity at the position of our samples was measured and calibrated by a light intensity detector (Thorlabs PM100D with S401C detector).

Structural Characterization.

Surface and cross section morphology was observed by scanning electron microscope (SEM) using Hitachi S-4800 microscope. The surface temperature, infrared images and video in this work was recorded by infrared thermal imager (Ti 100, FLUKE; V5.5.14, HIKMICRO).

Table S1. Comparison of this work with the typical/record performance of previously reported PV-PEC tandem cell for solar water splitting.[1-20]

List*	Typical photoelectrode	Tandem cell modules	Electrode area, cm^2	Electrolyte/ pH	STH, %	Year	Ref
(1)	**GeSe**	**GeSe-TEG**	**16**	**1 M H_2SO_4**	**13.5**	**2022**	**This work**
(2)	TiO_2	TiO_2-PSG/Si	0.15	1 M KOH	6.6	2021	[1]
(3)	Fe_2O_3	Fe_2O_3-PSC	0.09	1M NaOH and 0.5M Na_2SO_3 pH 14	4.8	2021	[2]
(4)	Sb_2Se_3	Sb_2Se_3-2PSC	0.2	H_2SO_4 electrolyte, pH 1	10	2020	[3]
(5)	Si	Si-PSC	0.3	1 m H_2SO_4 electrolyte solution	17.6	2020	[4]
(6)	$BiVO_4$	$BiVO_4$-PSC	0.6	0.1 M phosphate-buffer, pH 7	3.1	2020	[5]
(7)	Cu_2O	Cu_2O-PSC	0.16	0.5 M Na_2SO_4, 0.1 M sodium phosphate	4.55	2020	[6]
(8)	$BiVO_4$	$BiVO_4$-PSC	0.25	0.1 m potassium borate buffer, 0.1 m K_2SO_4 electrolyte, pH 8	1.3	2020	[7]
(9)	$BiVO_4$	$BiVO_4$-PSC	1	1M borate buffer aqueous solution, pH 9.1	4.6	2019	[8]
(10)	Ta_3N_5	Ta_3N_5-CuInSe	0.84	0.2m aqueous potassium phosphate solution pH 13	7.7	2019	[9]
(11)	$BiVO_4$	$BiVO_4$-PSC	1	0.1 M phosphate buffer, pH 7.5	1	2018	[10]
(12)	Fe_2O_3	Fe_2O_3-a-Si-Pt 2jn	50	1 M KOH	0.6	2017	[11]
(13)	$BiVO_4$	$BiVO_4$-PSC	0.25	0.5 M phosphate buffer, pH 7	6.15	2016	[12]
(14)	$BiVO_4$-Fe_2O_3	$BiVO_4$-Fe_2O_3-2pSi	5	0.5 phosphate buffer,0.5M Na_2SO_3	7.7	2016	[13]
(15)	Fe_2O_3	Fe_2O_3-PSC	0.12	1 M NaOH	2.4	2015	[14]
(16)	$CuIn_xGa_{1-x}Se_2$	CIGS-PSC	0.2	0.5 M H2SO4, pH 0	6.3	2015	[15]
(17)	Cu_2O	Cu_2O-PSC	0.057	0.5 M K_2SO_4, pH 5	2.5	2015	[16]
(18)	$BiVO_4$	$BiVO_4$-2jn Ⅲ/Ⅴ	0.16	0.5 M phosphate buffer, pH 7	8.1	2015	[17]
(19)	$BiVO_4$	$BiVO_4$-2jn Si	0.283	0.1M potassium phosphate, pH 7.3	5.2	2014	[18]
(20)	$BiVO_4$	$BiVO_4$-2jn Si	1	0.1M potassium phosphate, pH 7.3	4.9	2013	[19]
(21)	Fe_2O_3	Fe_2O_3-DSSC	0.196	1 M NaOH, pH 13.6	1.17	2012	[20]
(22)	WO_3	WO_3-DSSC	0.196	1 M HClO4, pH 0	3.1		[21]

* Reported are cited chronologically.

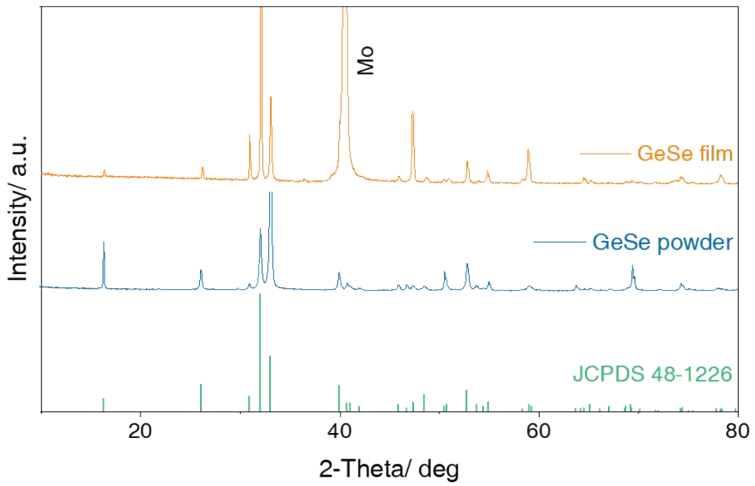

Figure S1. XRD pattern of the GeSe film and purchased GeSe powder.

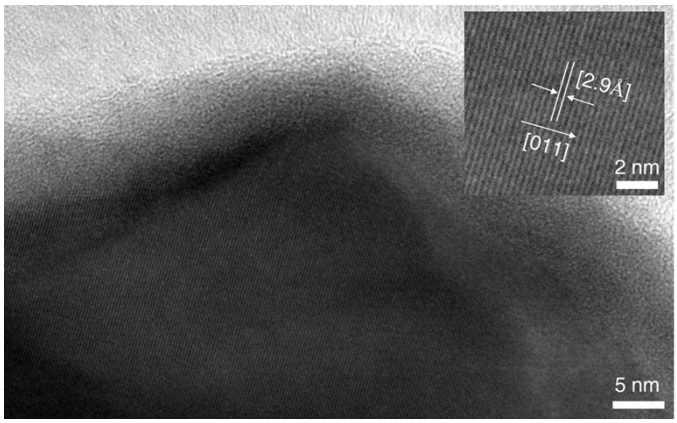

Figure S2. Lattice images of the GeSe MABs crytal.

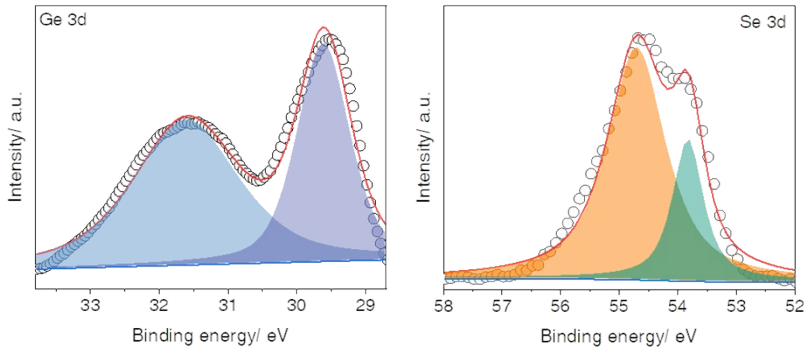

Figure S3. XPS spectra of GeSe MABs. Scatter points represent the original experimental data, whereas solid lines represent fitted curves.

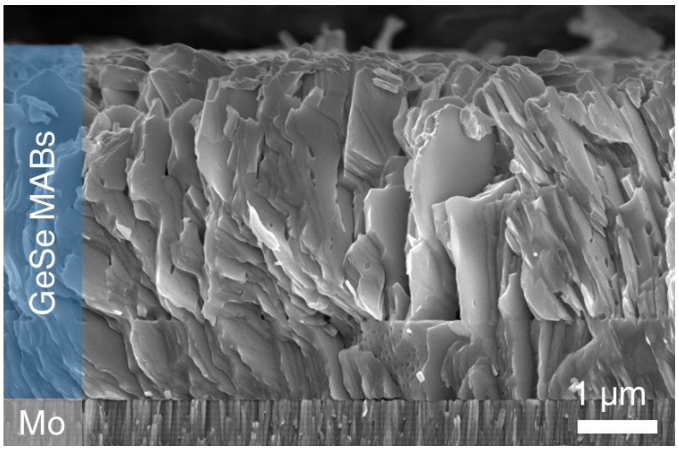

Figure S4. Cross-section morphology of GeSe micro air brick.

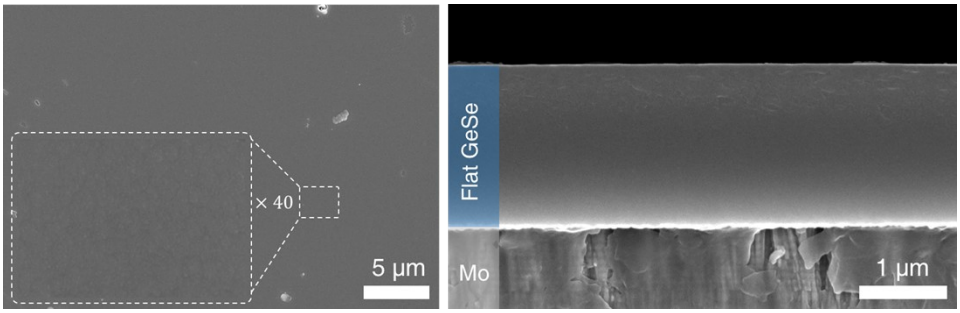

Figure S5. Surface and cross-section morphology of flat GeSe film.

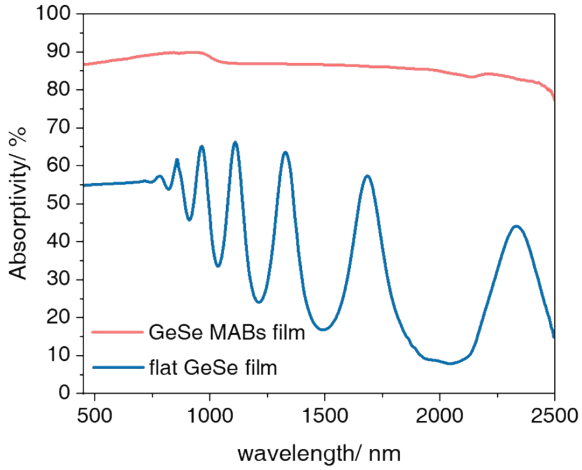

Figure S6. Light absorptivity spectrum of GeSe MABs film and flat GeSe film.

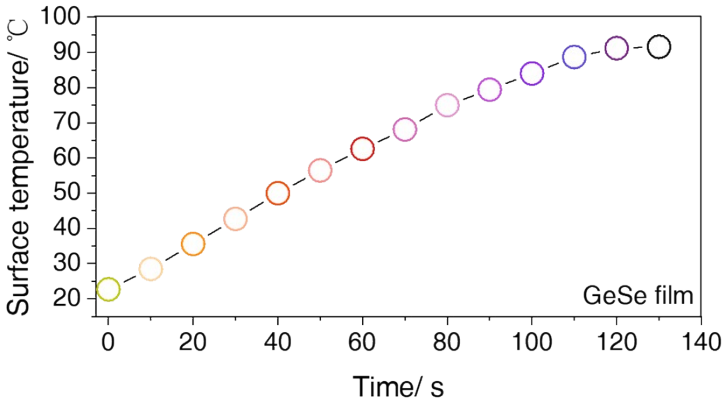

Figure S7. Surface light induced heating responding curve of the GeSe MABs loaded on Mo sheet.

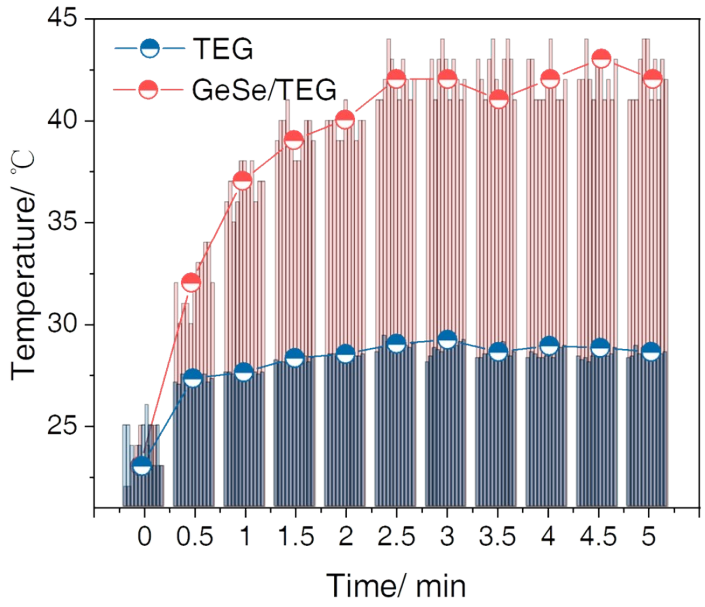

Figure S8. Statistical histogram and average temperature change curve of the surface temperature of 10 GeSe/TEG samples in various illumination time.

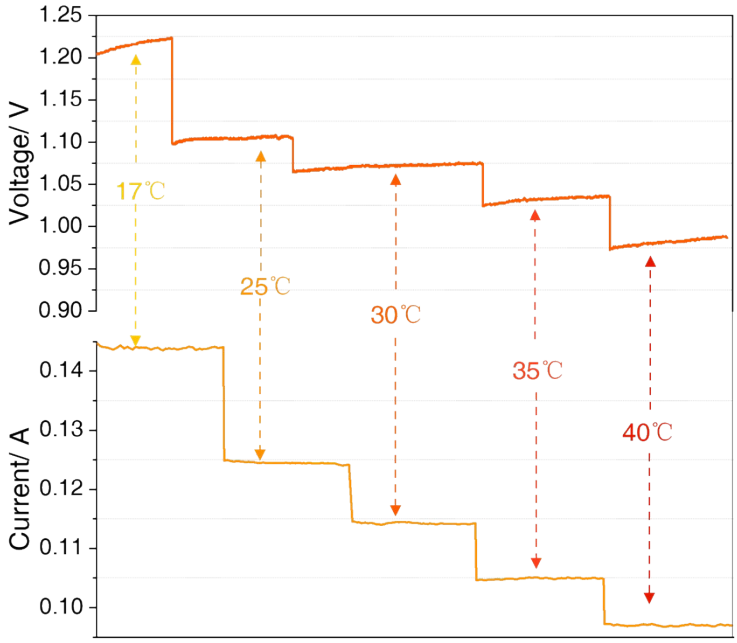

Figure S9. Output voltage and current of the GeSe/TEG photothermovoltaic cell in vary temperature of coolant.

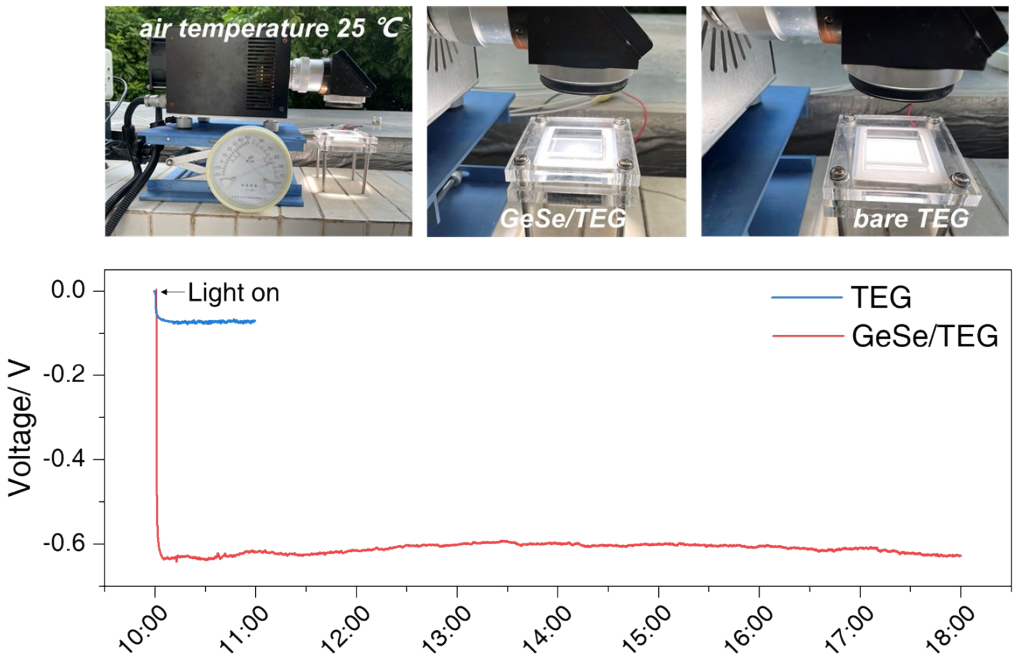

Figure S10. Optical picture and output voltage of GeSe/TEG and bare thermoelectrical generator in outdoor with air as the coolant.

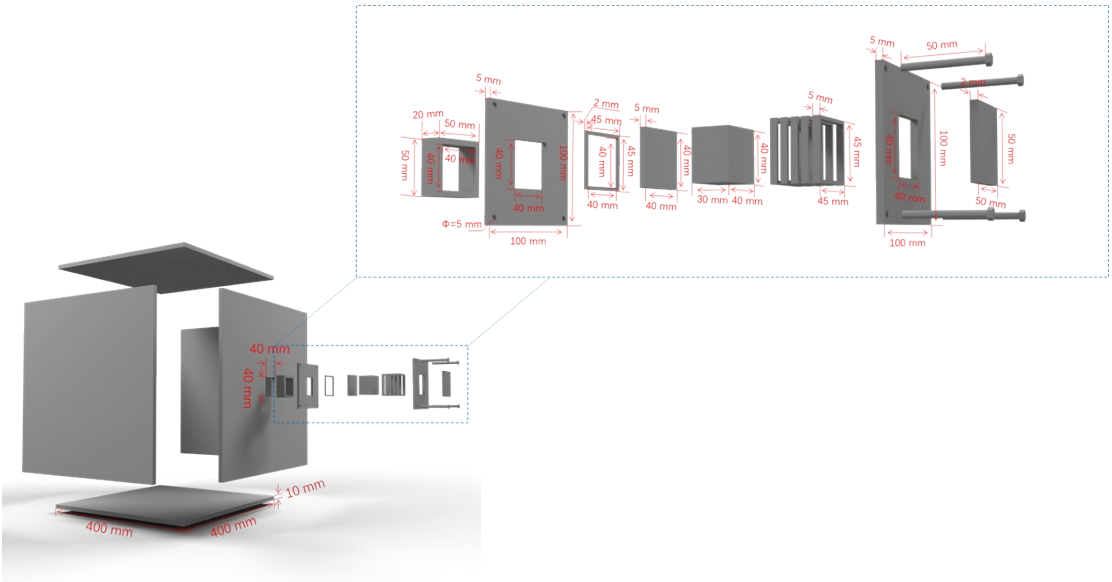

Figure S11. Diagram of geometric dimension of the Pt/TiO_2/GeSe/TEG overall solar water splitting device.

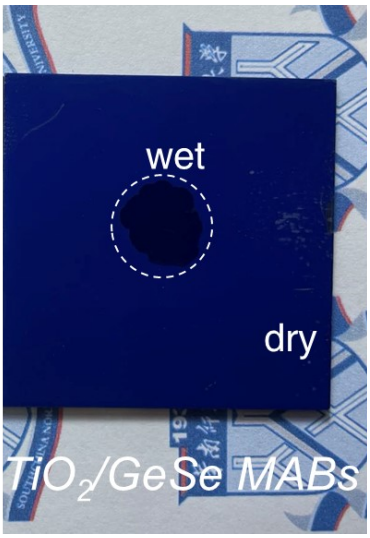

Figure S12. Photograph of the TiO_2/GeSe MABs film in dry and wet state.

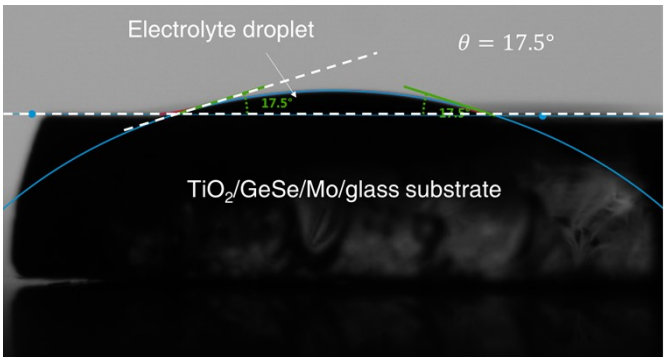

Figure S13. Surface contact angles of electrolyte droplets on TiO_2/GeSe samples.

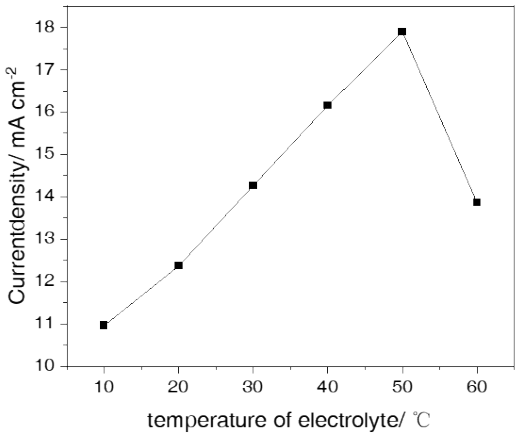

Figure S14. Statistical diagram for the saturated photocurrent density under 1.52 V vs C.E. in vary temperature electrolyte.

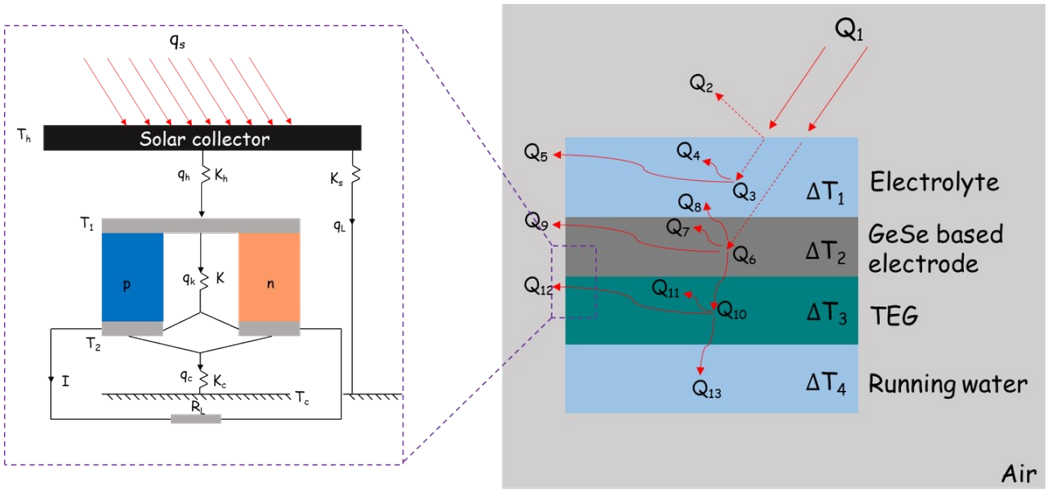

Figure S15. The schematic diagram of thermal energy storage and conversion for GeSe/TEG hybrid device. Schematic diagram of a solar-driven thermoelectric generator was shown in inset.

The schematic diagram of a solar-driven thermoelectric generator of the core thermal energy conversion and storage part (GeSe/TEG) was shown in left inset of FigureS15.[25] Although the full solar spectrum can be exploited by combining thermoelectric modules and solar thermal captured electrode, the efficiency enhancement of hybrid system is still modest. This is mainly due to the limitations of present integrated designs, which cannot provide sufficient temperature gradients on the thermoelectric modules to deliver meaningful voltage.[26, 27] In some previous reports, they have not only focused on the development of high-efficiency, low-cost thermoelectric modules, but also the utilization of concentrated solar light to enhance the thermal effect and optimization of the integrated design to maximize temperature gradients and heat transfer.[28, 29] Such as the model in inset of FigureS15, it can guide us to further optimize the parameters of solar-driven thermoelectric generator (including efficiency, power output, and load resistance) according to the engineering design ideas.

Where $\mathbf{Q_1}$ is the total input solar radiation energy; $\mathbf{Q_2}$ is Part of the solar energy reflected by water; $\mathbf{Q_3}$ is solar energy input into the electrolyte; $\mathbf{Q_4}$ is the energy absorbed by water; $\mathbf{Q_5}$ is the energy lost to the air from electrolyte; $\mathbf{Q_6}$ is solar energy input into the GeSe based electrode; $\mathbf{Q_7}$ is the energy absorbed by GeSe based electrode; $\mathbf{Q_8}$ is the energy transferred from GeSe (hot end) to end electrolyte (cold end); $\mathbf{Q_9}$ is the energy lost to the air from GeSe based electrode; $\mathbf{Q_{10}}$ is the energy input to TEG; $\mathbf{Q_{11}}$ is the energy absorbed by TEG; $\mathbf{Q_{12}}$ is the energy lost to the air from TEG; $\mathbf{Q_{13}}$ is the energy input to running water.

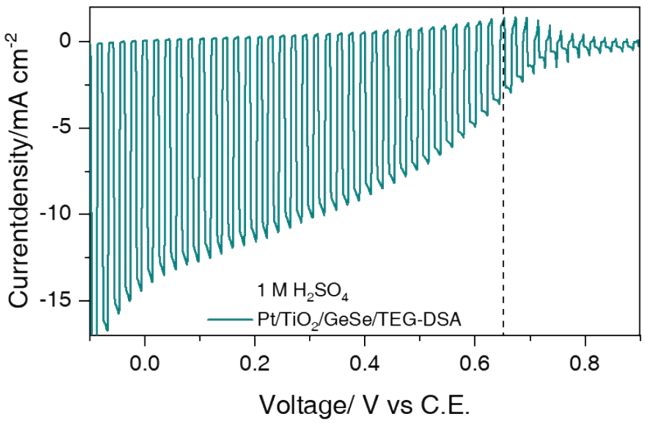

Figure S16. J-V curve of Pt/TiO_2/GeSe/TEG and DSA electrode in two electrode configuration in 1 M H_2SO_4 solution.

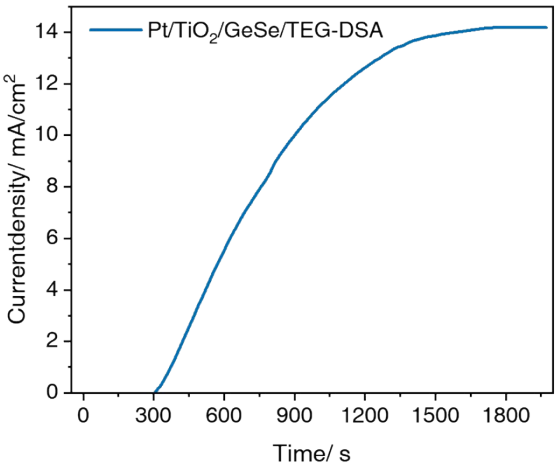

Figure S17. Current density-time plot of Pt/TiO_2/GeSe/TEG and DSA electrode in preheating process for 1500 s in 1 M H_2SO_4 solution.

Table S2. Comparison of this work with the previously reported TE and photothermal materials

hybrid solar water splitting device.[21-24]

List	Light absorbing materials	Highest surface temperature/ ℃	Configuration	Type of water splitting device	Performance evaluation criteria	Ref.
(1)	GeSe film	92	GeSe(-)-DSA(+)-TE	PEC-TE	STH efficiency ~13.5% after light soaking accumulated process of 1500 s	This work
(2)	electrolyte	N/A	$BiVO_4$(+)-Si(-)-TE	PEC-TE	improved overall water splitting activity of 1.6 times	Cheng et. al Sci. Bull. 2020 [22]
(3)	Ni Nanosheets Array	92.2	NiFe-LDH/CFC/TE (+) // Ni NSs/TE (-)	Electrolyzer-TE hybrid device	N/A	Liu et. al Nano energy 2018 [23]
(4)	Ni@NCNTs/NF-L	56.8	(−) Ni@NCNTs/NF-L/TE // NiFe-L (+)	Electrolyzer-TE hybrid device	STH efficiency ~5.1%	Zhou et. al Appl. Catal. B 2020 [24]

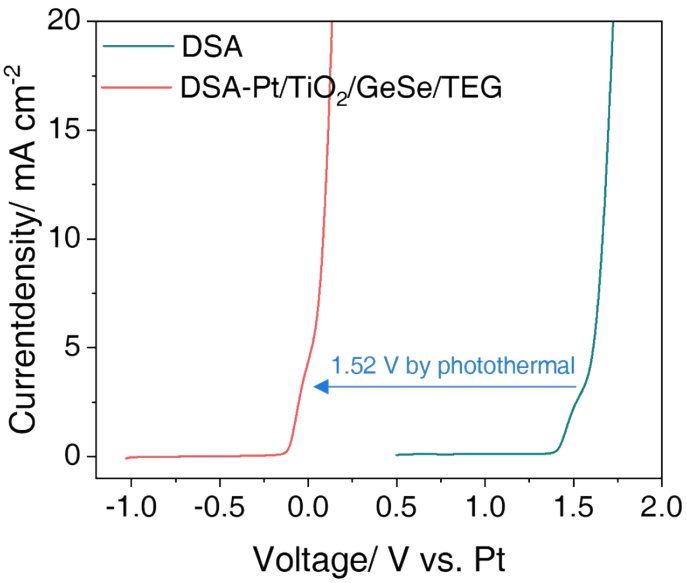

Figure S18. J-V curve of Pt sheet and Pt/TiO_2/GeSe/TEG connected to DSA in 1 M H_2SO_4 solution in the form of two electrodes.

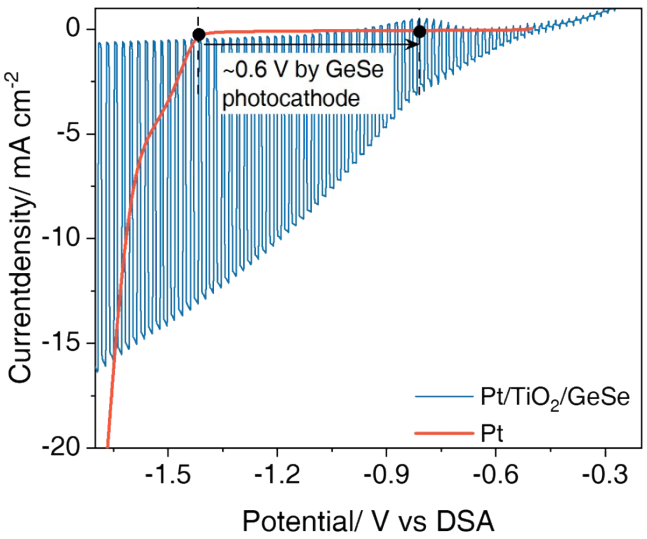

Figure S19. J-V curves of the Pt/TiO_2/GeSe and Pt in two electrode configuration with DSA in 1 M H_2SO_4 solution, respectively.

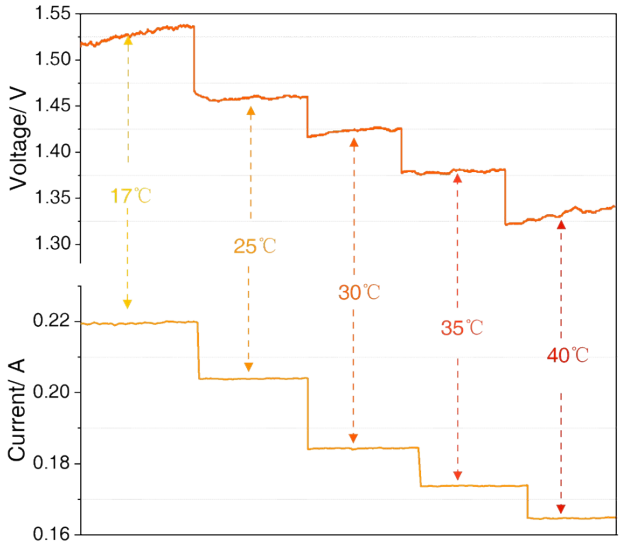

Figure S20. Output voltage and current of the Pt/TiO_2/GeSe/TEG photothermovoltaic cell in vary temperature of running water.

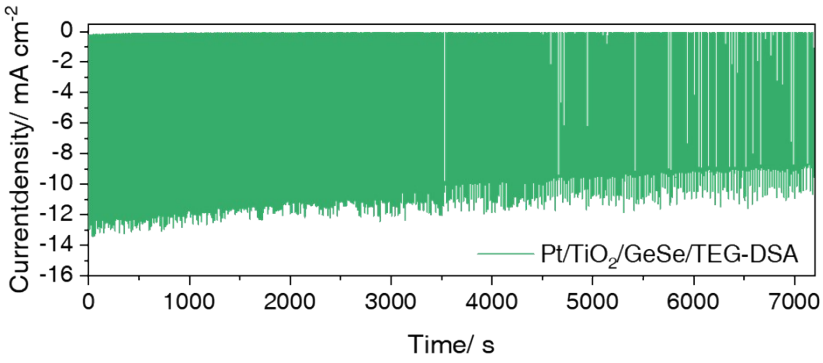

Figure S21. Current density-time curve of Pt/TiO_2/GeSe/TEG device.

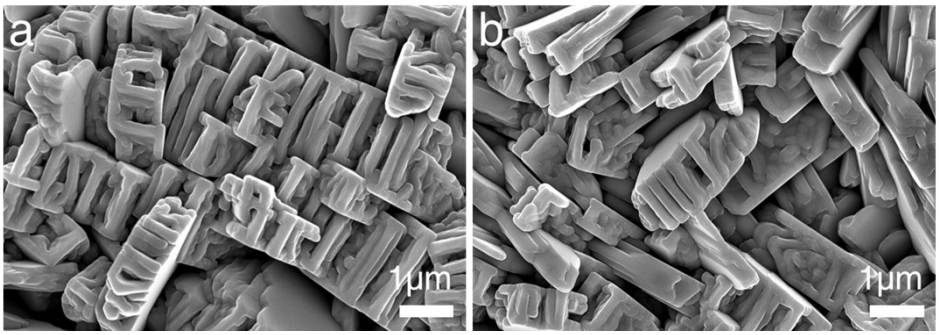

Figure S22. The surface morphology of GeSe photoelectrodes before (a) and after (b) stability test.

From Fig. S22, we did not find any obvious differences in the structural of the GeSe based device before and after stability test.

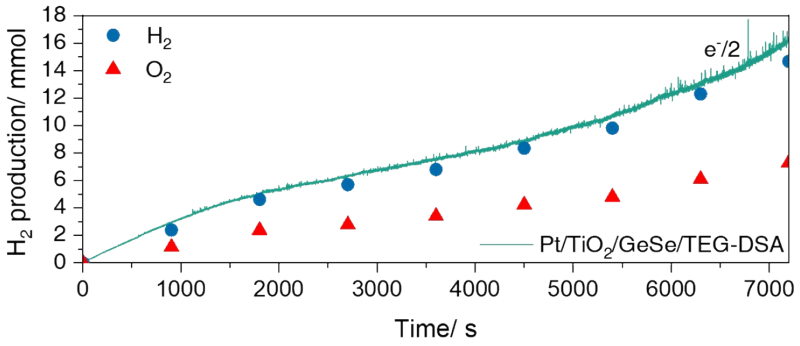

Figure S23. GC analysis of Pt/TiO_2/GeSe/TEG-DSA unbiased solar water splitting cell in 1 M H_2SO_4 buffer solution with 100 mW/cm^2 illumination.

Reference

1 S. E. Jun, S. P. Hong, S. Choi, C. Kim, S. G. Ji, I. J. Park, S. A. Lee, J. W. Yang, T. H. Lee and W. Sohn, *Small*, 2021, **17**, 2103457.

2 K.-Y. Yoon, J. Park, M. Jung, S.-G. Ji, H. Lee, J. H. Seo, M.-J. Kwak, S. Il Seok, J. H. Lee and J.-H. Jang, *Nat. Commun.*, 2021, **12**, 1-12.

3 W. Yang, J. Park, H.-C. Kwon, O. S. Hutter, L. J. Phillips, J. Tan, H. Lee, J. Lee, S. D. Tilley and J. D. Major, *Energy Environ. Sci.*, 2020, **13**, 4362-4370.

4 S. K. Karuturi, H. Shen, A. Sharma, F. J. Beck, P. Varadhan, T. Duong, P. R. Narangari, D. Zhang, Y. Wan and J. H. He, *Adv. Energy Mater.*, 2020, **10**, 2000772.

5 S. Zhang, L. Shen, T. Ye, K. Kong, H. Ye, H. Ding, Y. Hu and J. Hua, *Energy & Fuels*, 2020, **34**, 5016-5023.

6 L. Pan, Y. Liu, L. Yao, D. Ren, K. Sivula, M. Grätzel and A. Hagfeldt, *Nat. Commun.*, 2020, **11**, 1-10.

7 C. Pornrungroj, V. Andrei, M. Rahaman, C. Uswachoke, H. J. Joyce, D. S. Wright and E. Reisner, *Adv. Funct. Mater.*, 2021, **31**, 2008182.

8 X. Li, M. Jia, Y. Lu, N. Li, Y.-Z. Zheng, X. Tao and M. Huang, *Electrochim. Acta*, 2020, **330**, 135183.

9 T. Higashi, H. Nishiyama, Y. Suzuki, Y. Sasaki, T. Hisatomi, M. Katayama, T. Minegishi, K. Seki, T. Yamada and K. Domen, *Angew. Chem.*, 2019, **131**, 2322-2326.

10 X. Shi, H. Jeong, S. J. Oh, M. Ma, K. Zhang, J. Kwon, I. T. Choi, I. Y. Choi, H. K. Kim and J. K. Kim, *Nat. Commun.*, 2016, **7**, 1-6.

11 A. Vilanova, T. Lopes, C. Spenke, M. Wullenkord and A. Mendes, *Energy Storage Mater.*, 2018, **13**, 175-188.

12 Y. Qiu, W. Liu, W. Chen, W. Chen, G. Zhou, P.-C. Hsu, R. Zhang, Z. Liang, S. Fan and Y. Zhang, *Sci. Adv.*, 2016, **2**, e1501764.

13 J. H. Kim, J.-W. Jang, Y. H. Jo, F. F. Abdi, Y. H. Lee, R. Van De Krol and J. S. Lee, *Nat. Commun.*, 2016, **7**, 1-9.

14 D. Sabba, M. H. Kumar, L. H. Wong, J. Barber, M. Grätzel and N. Mathews, *Nano Lett.*, 2015, **15**, 3833-3839.

15 J. Luo, Z. Li, S. Nishiwaki, M. Schreier, M. T. Mayer, P. Cendula, Y. H. Lee, K. Fu, A. Cao and M. K. Nazeeruddin, *Adv. Energy Mater.*, 2015, **5**, 1501520.

16 P. Dias, M. Schreier, S. D. Tilley, J. Luo, J. Azevedo, L. Andrade, D. Bi, A. Hagfeldt, A. Mendes and M. Grätzel, *Adv. Energy Mater.*, 2015, **5**, 1501537.

17 Y. Pihosh, I. Turkevych, K. Mawatari, J. Uemura, Y. Kazoe, S. Kosar, K. Makita, T. Sugaya, T. Matsui and D. Fujita, *Sci Rep*, 2015, **5**, 1-10.

18 L. Han, F. F. Abdi, R. van de Krol, R. Liu, Z. Huang, H. J. Lewerenz, B. Dam, M. Zeman and A. H. Smets, *ChemSusChem*, 2014, **7**, 2832-2838.

19 F. F. Abdi, L. Han, A. H. Smets, M. Zeman, B. Dam and R. Van De Krol, *Nat. Commun.*, 2013, **4**, 1-7.

20 J. Brillet, J.-H. Yum, M. Cornuz, T. Hisatomi, R. Solarska, J. Augustynski, M. Graetzel and K. Sivula, *Nat. Photonics*, 2012, **6**, 824-828.

21 H. Cai, W. Zhao, G. Xiao, Y. Hu, X. Wu, H. Ni, S. Ikeda, Y. Ng, J. Tao and L. Zhao, *Adv. Sci.*, 2022, 2205726.

22 Y. Kang, R. Chen, C. Zhen, L. Wang, G. Liu and H.-M. Cheng, *Sci. Bull.*, 2020, **65**, 1163-1169.

23 L. Zhao, Z. Yang, Q. Cao, L. Yang, X. Zhang, J. Jia, Y. Sang, H.-J. Wu, W. Zhou and H. Liu, *Nano Energy*, 2019, **56**, 563-570.

24 H. Yuan, F. Liu, G. Xue, H. Liu, Y. Wang, Y. Zhao, X. Liu, X. Zhang, L. Zhao and Z. Liu, *Appl. Catal. B-Environ.*, 2021, **283**, 119647.

25 J. Chen, *J. Appl. Phys.*, 1996, **79**, 2717-2721.

26 D. Yang and H. Yin, *IEEE Trans. Energy Convers.*, 2011, **26**, 662-670.

27 Q. Wang, C. Pornrungroj, S. Linley and E. Reisner, *Nat. Energy*, 2022, **7**, 13-24.

28 P. Tomeš, C. Suter, M. Trottmann, A. Steinfeld and A. Weidenkaff, *J. Mater. Res.*, 2011, **26**, 1975-1982.

29 D. Kraemer, Q. Jie, K. McEnaney, F. Cao, W. Liu, L. A. Weinstein, J. Loomis, Z. Ren and G. Chen, *Nat. Energy*, 2016, **1**, 1-8.